Title

Operation-Induced BiVO4 Surface Reconstruction Modulates Photoelectrochemical Glycerol Photooxidation Stability and Activity

Journal

ACS Energy Letters

ISSN

2380-8195

Authors

Yang, Jin Wook

Kwon, Hee Ryeong

Kim, Dong Su

et al.

Publication Date

2026-08-04

DOI

10.1021/acsenergylett.6c01409

Operation-Induced $BiVO_4$ Surface Reconstruction Modulates Photoelectrochemical Glycerol Photooxidation Stability and Activity

Jin Wook Yang[1,2,4,‡], Hee Ryeong Kwon[4,‡], Dong Su Kim[1,2], Nicole A. Sagui[1,2,3], Yun Jeong Hwang[5], Ho Won Jang[4,6,*], Shannon W. Boettcher[1,2,3,*]

[1]Department of Chemical & Biomolecular Engineering and Department of Chemistry, University of California, Berkeley, CA 94720, United States

[2]Energy Technologies & Systems Division, Lawrence Berkeley National Laboratory, Berkeley, CA 94720, United States

[3]Oregon Center for Electrochemistry, Department of Chemistry and Biochemistry, University of Oregon, Eugene, OR 97403, United States

[4]Department of Materials Science and Engineering, Research Institute of Advanced Materials, Seoul National University, Seoul 08826, Republic of Korea

[5]Department of Chemistry, Seoul National University, Seoul 08826, Republic of Korea

[6]Advanced Institute of Convergence Technology, Seoul National University, Suwon 16229, Republic of Korea

*Email: boettcher@berkeley.edu; hwjang@snu.ac.kr

ABSTRACT

Operation-induced surface reconstruction of photoelectrodes is underexplored as a path to control stability and performance. We show how adaptive junctions form via surface reconstruction of $BiVO_4$ during glycerol photooxidation and how these surfaces affect electrolyte-dependent kinetics and durability. Preferential V dissolution in both acidic and alkaline media forms a Bi-rich layer. *In situ* measurements through a dual-working-electrode platform quantify the changes in photovoltage and charge-transfer resistance derived from adaptive junction formation, while enabling quantitative separation of the driving forces for charge separation and interfacial catalysis. The reconstructed surface in acidic media improves hole-transfer kinetics, functions as a glycerol-oxidation catalyst, and imparts photostability. Surface reconstruction in alkaline media exhibits the opposite behavior, impeding hole injection. This instability is mitigated by trace Ni^{2+} ions, which drive *in situ* surface activation without cocatalyst pre-deposition. This study shows the significance of surface reconstruction in the design of durable photoelectrodes for applications targeting organic electro-oxidation.

Photoelectrochemical (PEC) energy conversion is a platform to generate fuels and chemicals using light as an input.[1–3] The photovoltage generated by a semiconductor contributes to the free-energy needed to drive the desired reaction, and, if large enough, enables a configuration without external bias.[4–7] A common limitation is the need to drive the four-electron oxygen evolution reaction (OER), which has both a large positive thermodynamic potential and slow kinetics.[8] The oxidizing potential for OER also contributes to the degradation of PEC systems, as many semiconductors are unstable under oxidizing conditions.[9] The use of alternative anodic reactions, like biomass oxidations, provides one route to lower the voltage required for the anode reaction and increase stability.[10–14]

Glycerol, produced as a byproduct at ~10 wt% during biodiesel production, is widely studied as an alternative anodic reaction, as it can be converted into C_3 products with ~150-fold higher value than the reactant.[15,16] Compared with OER, the glycerol oxidation reaction (GOR) has a lower thermodynamic potential and faster kinetics, both of which can reduce the required photovoltage when coupled with a cathodic reaction and improve the stability.[4] The GOR has been coupled with the cathodic hydrogen evolution reaction,[17] as well as the oxygen,[18] carbon-dioxide,[19] and nitrate[20,21] reduction reactions in photoelectrochemical architectures. Noble metals with low overpotential for GOR have been integrated onto semiconductors to couple the photovoltage to GOR.[22–25] The GOR has also been performed directly on the semiconductor surface without cocatalysts, presumably with the reaction taking place on reconstructed surfaces.[26,27]

Bismuth vanadate ($BiVO_4$) is among the most-studied semiconductors for GOR, because Bi–O bonding is thought to be a suitable adsorption site for glycerol.[28] As a light absorber, the 2.4 eV band gap (E_g) balances the trade-off between photocurrent and photovoltage, enabling both visible-light absorption and photovoltage generation, although the obtained photovoltages so far are below

the practical recombination limit of $qV_{oc} \approx E_g - 0.4$ eV.[29–31] $BiVO_4$ has thus been extensively studied with a focus on improving GOR performance through the engineering of morphology,[32] orientation,[33,34] surface composition,[35,36] doping,[37–39] vacancies,[40] and electrolyte.[41,42] However, despite the importance of surface chemical and structural changes to the physics of charge recombination and electrochemical catalysis,[43] there have been no studies of the surface reconstructions of $BiVO_4$ during GOR and their resulting impact on stability under different reaction environments.

Here, we show that $BiVO_4$ forms adaptive junctions with electrolyte under GOR conditions through a dynamic operation-induced surface reconstruction. We find that the interface kinetics are modulated in response to the electrolyte environment, which also affects the GOR stability. We use a dual-working electrode (DWE) platform to separate bulk and surface potentials of $BiVO_4$ and for the *in-situ* photovoltage measurement at the semiconductor|catalyst (sem|cat) interface.

The fabrication process of the $BiVO_4$ film consists of two steps: electrodeposition of a BiO_x film followed by the thermal reaction with $VO(C_5H_7O_2)_2$ (Figure S1). X-ray diffraction (XRD) patterns showed that the $BiVO_4$ layer was fully crystallized into the monoclinic phase (Figure S2). The 400-nm-thick $BiVO_4$ film consisted of densely packed grains of a few hundred nanometers in size (Figure S3).

The PEC water and glycerol oxidation response of $BiVO_4$ was evaluated under acidic (pH = 2, sulfate buffer solution), as well as alkaline (pH = 9, borate buffer solution) conditions, both with and without 0.10 M glycerol. Current density–potential (*J–E*) plots in both electrolytes reveal a cathodic shift of the onset potential and increased photocurrent density upon glycerol addition (Figure 1a). The electrolytes with glycerol also yield more-negative open-circuit potential (OCP) values compared to water oxidation under both conditions, consistent with the more-negative

thermodynamic redox potential for glycerol than water (Figure S4). An enhancement in the pseudo fill factor (pFF) observed under acidic and alkaline conditions shows higher rates of the $BiVO_4$ photoanode toward GOR compared to OER at the same potentials (Figure S5). Potentiostatic impedance spectroscopy (PEIS) was measured over 0.3–1.2 V_{RHE}, and the Nyquist plots were fitted to a Randles circuit (Figure S6). As shown in Table S1, the charge transfer resistance (R_{ct}) toward GOR is lower than that for OER across most of the potential range, with a pronounced drop in R_{ct} observed at more cathodic potentials (0.3–0.5 V_{RHE}), reflecting fast charge transfer for GOR. The faster oxidation kinetics have been found previously,[28,44] and are observed across different pH conditions (Figure S7). However, the stability of the $BiVO_4$ photoanode driving GOR at different pH conditions has not been previously investigated.

The PEC GOR stability test of the $BiVO_4$ photoanode was carried out at 1.23 V_{RHE} in both pH = 2 and pH = 9 conditions (Figure 1b). At pH = 2, the initial photocurrent increased with time and saturated, whereas it rapidly decayed without recovery at pH = 9. These data show that the initial surface, which is favorable for hole collection and catalysis, evolves in opposite ways depending on pH. Despite these different photoelectrochemical responses with time, scanning electron microscopy (SEM) images of the $BiVO_4$ surface after each 1-h operation reveal similar microstructural changes in both pH environments, including increased roughness and corrosion at grain boundaries.

To investigate surface-composition changes for the $BiVO_4$ during the reaction, elemental dissolution rates were obtained by analyzing the electrolyte via inductively coupled plasma mass spectrometry (ICP-MS) after the stability test (Figure 1c). For OER, the positive thermodynamic potential and slow kinetics cause surface hole accumulation, leading to the leaching of vanadate species.[45] Thus, at both pH = 2 and pH = 9, the dissolution rate of V was significantly higher than

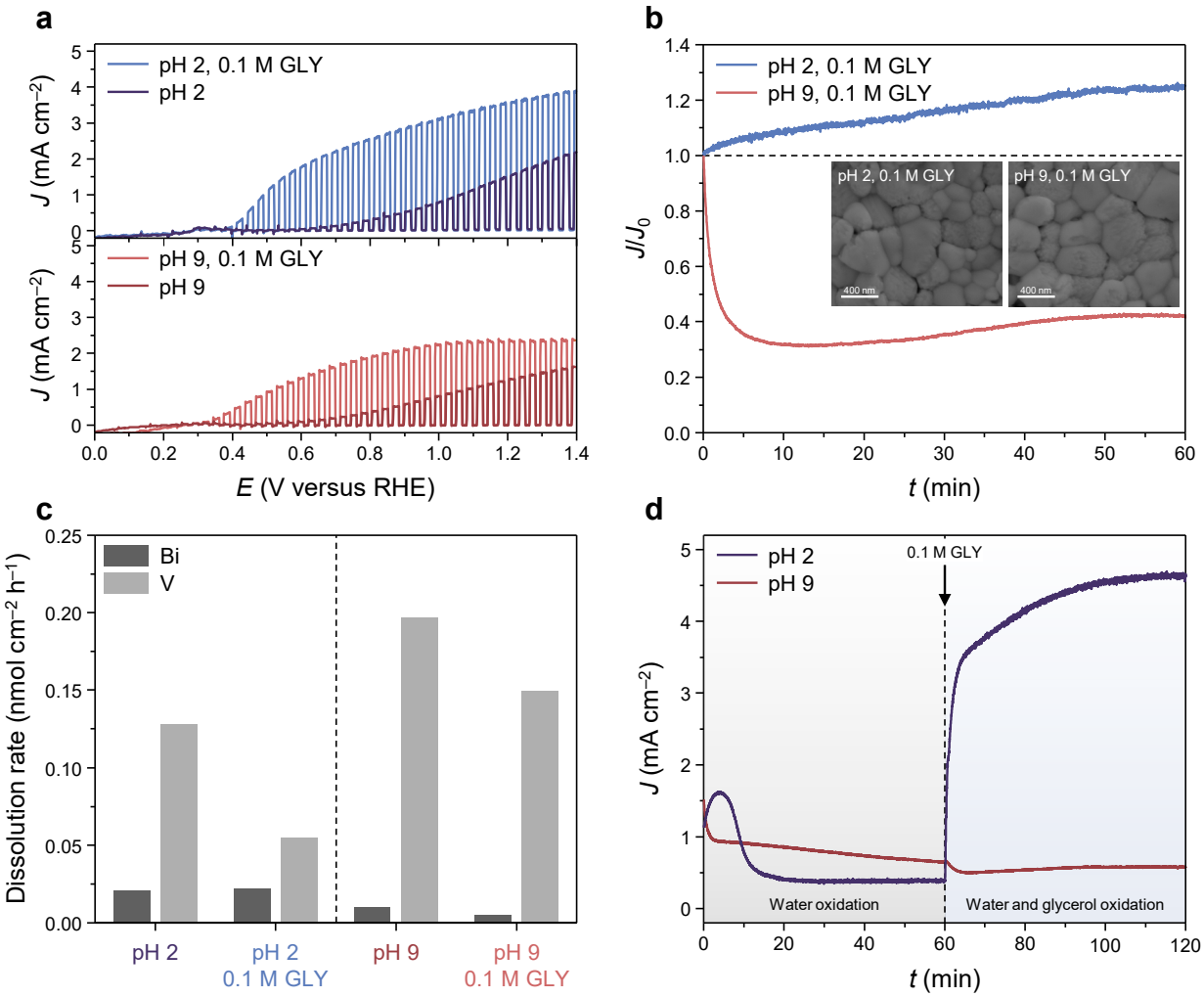

Figure 1. Photoelectrochemical water and glycerol oxidations at acidic and alkaline conditions. (a) *J*–*E* plots of $BiVO_4$ photoanodes in water and glycerol oxidations. (b) Normalized *J*–*t* plots of $BiVO_4$ photoanodes in glycerol oxidation. Inset: SEM images of $BiVO_4$ after a 1-h stability test of glycerol oxidation. (c) Elemental dissolution rates in water and glycerol oxidations. (d) *J*–*t* plots of $BiVO_4$ photoanode at 1.23 V_{RHE} in water oxidation, followed by glycerol addition.

that of Bi, which also correlated with the photocurrent decay observed in the OER current density–time (*J*–*t*) plots (Figure S8). Despite the faster kinetics of GOR, a significant degree of V leaching was still observed, although to a lesser extent than for the OER. These results suggest that both the enhanced acidic GOR and the diminished alkaline GOR were the result of compositional change to the Bi-rich surface due to V dissolution during the operation.

To investigate the effect of compositional change on glycerol oxidation behavior, 0.10 M glycerol was added to the electrolyte during the PEC stability test, and the photocurrent response was monitored (Figure 1d). At pH = 2, the initially degraded photocurrent during the first hour recovered rapidly and remained stable upon glycerol addition. In contrast, at pH = 9, the photocurrent continued to decrease without recovery, revealing that the Bi-rich surface led to distinct catalytic activity for GOR depending on pH, thereby contributing to stability differences. In *J–t* plots of the $BiVO_4$ photoanode measured by sequentially replacing the GOR electrolyte every hour, the photocurrent reached a new saturated value within ~1 h, suggesting that the surface reconstruction approaches a quasi-steady state under each pH condition (Figure S9). The decreased photocurrent observed at pH = 9 was recovered when switched to the pH = 2 electrolyte. The smaller original photocurrent returned upon switching back to the pH = 9 electrolyte. This indicates that the Bi-rich surface undergoes dynamic reconstruction depending on the pH, leading to changes in surface catalytic activity and junction properties.

To investigate the effect of electrolyte conditions on surface changes in $BiVO_4$, *ex situ* analyses were performed on the photoanodes after 1-h GOR stability tests. The XRD analysis shows that most diffraction patterns are retained with only a slight decrease in peak intensity, indicating the bulk $BiVO_4$ phase is largely preserved (Figure S10). High-resolution transmission electron microscopy (HR-TEM) images also show that the monoclinic phase of $BiVO_4$ was retained in the bulk (Figure 2a). At the surface, a ~3-nm-thick amorphous Bi-rich layer was observed after GOR at pH = 2.

To study the surface reconstruction, electron energy loss spectroscopy (EELS) analysis was used in combination with high-angle annular dark-field scanning transmission electron microscopy (HAADF-STEM) imaging (Figure 2b). The V $L_{2,3}$-edge peaks progressively shifted by 0.83 and

0.60 eV to higher energy losses from the surface toward the bulk, respectively. These results indicate that acidic GOR drives surface reconstruction over a depth of several nanometers. This result can be explained by V species dissolution and the accompanying formation of O vacancies within the reconstructed surface, leading to a reduction in the valence of V^{5+} to maintain charge neutrality.[46,47]

After GOR at pH = 9, a ~6-nm-thick Bi-rich layer was observed on the crystalline $BiVO_4$ (Figure 2c). The thicker and denser overlayer formed at pH = 9 compared to pH = 2 originates from the tendency of Bi to exist as hydroxides with abundant OH^- under alkaline conditions, which is consistent with the layered Bi-rich structure that is characteristic of hydroxides.[48] The EELS data showed a shift of 0.9 and 1.3 eV toward higher energy losses for the V $L_{2,3}$-edge peaks going from surface to bulk, and the peak intensities decreased in the surface region (Figure 2d). Compared to pH = 2, the larger peak shift and intensity decrease at pH = 9 suggest more-significant V dissolution and surface reconstruction along with a more-distinct Bi-rich shell. Corresponding energy-dispersive X-ray spectroscopy (EDS) mapping from the HAADF-STEM image also displayed a thin V-deficient region of the Bi-rich/$BiVO_4$ sample obtained from acidic GOR (Figure S11). In contrast, a more-distinct V depletion was observed at the surface of Bi-rich/$BiVO_4$ subjected to alkaline GOR (Figure S12).

Within the potential range for the stability tests, the Pourbaix diagram of $BiVO_4$ indicates that only V species are substantially soluble at pH = 9, whereas both Bi and V are expected to be soluble species at pH = 2.[49] ICP-MS analysis shows that the dissolution rates at pH = 2 lead to more rapid V leaching compared to Bi, causing the formation of the thin Bi-rich layer (Figure 1c). At pH = 9, the faster V dissolution and suppressed Bi dissolution are also consistent with the Pourbaix diagram and the formation of the more-robust Bi-rich layer in alkaline media.

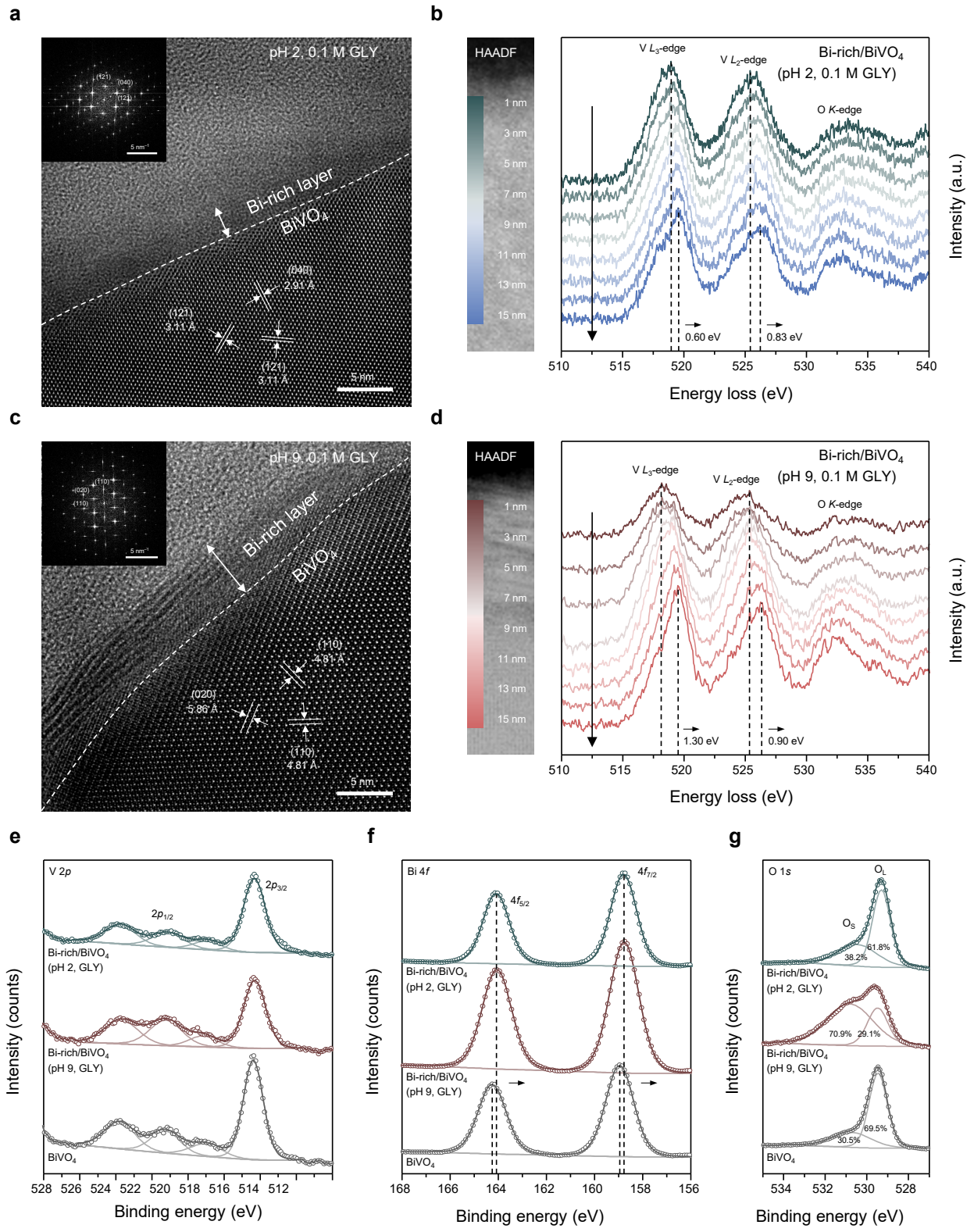

Figure 2. Characterization of $BiVO_4$ photoanodes after stability tests of acidic and alkaline glycerol oxidations. (a) HR-TEM image and FFT patterns of Bi-rich/$BiVO_4$ (pH = 2). (b) EELS spectra of the depth direction in a HAADF-STEM image of Bi-rich/$BiVO_4$ (pH = 2). (c) HR-TEM image and FFT patterns of Bi-rich/$BiVO_4$ (pH = 9). (d) EELS spectra of the depth direction in a HAADF-STEM image of Bi-rich/$BiVO_4$ (pH = 9). XPS (e) V 2*p*, (f) Bi 4*f*, and (g) O 1*s* spectra of pristine $BiVO_4$ and Bi-rich/$BiVO_4$ (pH = 2 and pH = 9).

To study the changes in surface composition and electronic structure, X-ray photoelectron spectroscopy (XPS) analysis was conducted on $BiVO_4$ before and after GOR operations. The V 2*p* spectra showed a reduced intensity in Bi-rich/$BiVO_4$, consistent with V leaching (Figure 2e). Also, the Bi $4f_{5/2}$ and $4f_{7/2}$ peaks shifted negatively from 164.26 and 158.96 eV to 164.13 and 158.83 eV at pH = 2, and further to 164.05 and 158.75 eV at pH = 9, respectively (Figure 2f). These shifts, accompanied by increased peak intensities, represent an increase in the local electron density around Bi atoms due to the depletion of V species.[50] The XPS-derived Bi:V ratio increased from 1.40 for pristine $BiVO_4$ to 2.25 and 3.80 after acidic and alkaline GOR, respectively, confirming preferential V depletion and operation-induced Bi enrichment at the surface (Table S2). In O 1*s* spectra, lattice oxygen (O_L) decreased from 70% to 62% at pH = 2 and further to 29% at pH = 9 (Figure 2g). This suggests that the surface reconstruction involves the modification of the local lattice-oxygen environment. The more pronounced decrease in O_L in alkaline media is consistent with stronger V dissolution, demonstrating characteristic differences in the Bi-rich layer depending on the electrolyte conditions.

To elucidate the origin of the electrolyte-dependent GOR stability of $BiVO_4$, we conducted *in situ* PEC measurements of Bi-rich/$BiVO_4$ photoanodes. In conventional three-electrode configurations, the photoelectrode is connected as a single working electrode (WE) through an ohmic back contact to the semiconductor. The limitation of these conventional measurements is that it is not possible to determine the relative contributions to voltage losses associated with the semiconductor relative to the surface catalytic process. We assume that the reconstructed surface, interacting with the electrolyte, is the site of the GOR catalysis and aim to understand the voltage changes associated with driving GOR on the reconstructed surface.

To study the individual components of the PEC system, we use a DWE platform, in which the Bi-rich layer formed during the operation was regarded as a GOR catalyst that could be independently evaluated. The DWE analysis was carried out comparing pristine $BiVO_4$ with Bi-rich/$BiVO_4$ photoanodes after 1-h chronoamperometry at pH = 2 and pH = 9, respectively. For the DWE device fabrication, 10-nm-thick Au was deposited on the surface of $BiVO_4$, forming a porous conductive layer, whose thickness was chosen to be electrolyte-permeable while ensuring electrical contact with the underlying catalyst layer (Figures 3a and S13).[51] WE1 and WE2 were connected to an ohmic back-contact at fluorine-doped tin oxide (FTO) and the front catalyst through the porous Au layer, respectively. The Au layer did not apparently contribute to the GOR activity within the potential range for DWE measurements (Figure S14). Therefore, the Au layer is taken to be in quasi-equilibrium with the catalyst potential and considered to function as an electrical contact for sensing E_{cat}. Due to the reduced optical transmittance by the Au layer, all measurements were conducted with back-side illumination (Figure S15).

Under illumination, the generated electron-hole pairs are separated by the semiconductor interface with the catalyst layer and electrolyte, causing a nonequilibrium state where the quasi-Fermi levels split. The hole quasi-Fermi level ($E_{F,p}$) drops below the electron quasi-Fermi level ($E_{F,n}$), and each converges toward the catalyst potential (E_{cat}) and the semiconductor potential (E_{sem}), respectively, generating a photovoltage at the sem|cat interface.[52] Quantifying the E_{cat} of the Bi-rich layer thus provides a direct measure of the sem|cat photovoltage, which is a key determinant of the PEC performance.

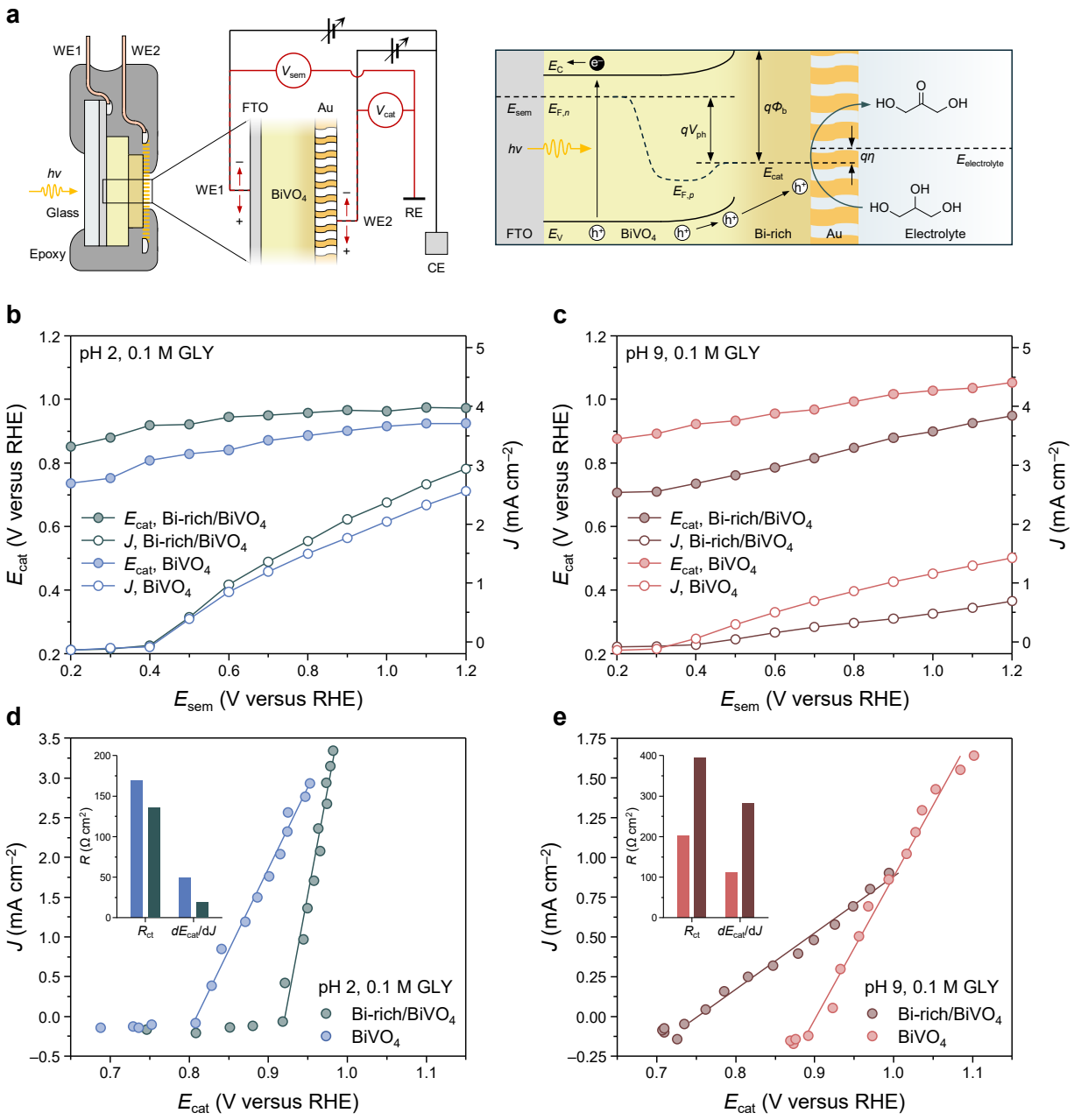

Figure 3. Dual-working electrode (DWE) measurements during photoelectrochemical glycerol oxidation. (a) Device schematic and band diagram of Bi-rich/$BiVO_4$ photoanode for DWE measurements. (b) E_{cat} and J versus E_{sem} for $BiVO_4$ photoanodes with or without a Bi-rich layer in a pH = 2 buffer solution with 0.10 M glycerol. (c) E_{cat} and J versus E_{sem} for $BiVO_4$ photoanodes with or without a Bi-rich layer in a pH = 9 buffer solution with 0.10 M glycerol. Note that in (b) the Bi-rich surface provides a higher photovoltage, given by $E_{cat} - E_{sem}$, which thus leads to a high catalytic current for GOR at a given $E_{sem,}$ but in (c) the Bi-rich surface provides a lower photovoltage, and thus a lower photocurrent at a given $E_{sem.}$ J–E_{cat} plots from DWE measurements of $BiVO_4$ and Bi-rich/$BiVO_4$ photoanodes in (d) pH = 2 and (e) pH = 9 buffer solutions with 0.10 M glycerol, which allow direct comparison of surface catalysis behavior. Inset: Comparison of R_{ct} at 0.60 V_{RHE} and dE_{cat}/dJ values of $BiVO_4$ and Bi-rich/$BiVO_4$ photoanodes. These data show that the surface reconstruction not only affects the PEC photovoltage but also the catalyst kinetics at a given $E_{cat,}$ and this result is supported by both DWE and impedance measurements.

While applying a stepwise potential scan from 0 to 1.3 V to WE1, we measured E_{cat} on the surface of $BiVO_4$ and Bi-rich/$BiVO_4$ at pH = 2 by independently sensing WE2 via the DWE configuration (Figure S16). The current density was simultaneously recorded as a response to E_{sem}, closely matching separately collected voltammetry (Figure S17). At pH = 2, the formation of the Bi-rich layer enhanced the photocurrent density and increased E_{cat} across the entire potential range (Figure 3b). Considering the difference between E_{sem} and E_{cat} is equivalent to the photovoltage, the Bi-rich layer is thus responsible for increasing the photovoltage for acidic GOR, also contributing to an increase in photostability of $BiVO_4$.

To determine the pH-dependent behavior of the Bi-rich layer, identical DWE measurements were conducted under alkaline conditions (Figures S18 and S19). The Bi-rich layer formed at pH = 9 decreased E_{cat}, thereby reducing both the photovoltage and photocurrent density of $BiVO_4$, which thus reflected a rapid degradation of alkaline GOR performance (Figure 3c). To compare the photovoltage trends, $E_{cat}-E_{sem}$ was plotted as a function of E_{sem} (Figure S20). For pristine $BiVO_4$, the $E_{cat}-E_{sem}$ values were larger at pH = 9 than at pH = 2, consistent with the pH-dependent trend in the OCP difference (Figure S4). The Bi-rich layer increased $E_{cat}-E_{sem}$ in acidic electrolyte but decreased $\underline{E}_{cat}-E_{sem}$ in alkaline electrolyte. Measurements without glycerol showed a decrease in photovoltage for both acidic and alkaline media, indicating an intrinsic instability of $BiVO_4$ for water oxidation regardless of pH (Figure S21).

Ultraviolet photoelectron spectroscopy (UPS) indicates that the Bi-rich layer slightly shifts the valence-band edge more negative relative to $BiVO_4$ (Figure S22). This trend is consistent with the reported dependence of $BiVO_4$ band alignment on surface stoichiometry.[53] Mott–Schottky measurements showed no significant changes to the flat band under both pH conditions (Figure

S23). Therefore, the hole-transfer characteristics of the Bi-rich layer are responsible for the different photostability with pH that cannot be explained by band-edge energetics.

Using the DWE platform, we analyzed the charge-transfer behavior of the Bi-rich layer at different pH conditions. First, PEIS analysis was conducted with and without the Bi-rich layer in a three-electrode configuration. After 1-h driving GOR at pH = 2, the Bi-rich/$BiVO_4$ shows an R_{ct} of 136 Ω cm^2, smaller than that of $BiVO_4$ (169 Ω cm^2), indicating that the Bi-rich layer promoted hole transfer for GOR (Figure S24). In contrast, the Bi-rich layer formed at pH = 9 shows increased R_{ct} from 203 to 394 Ω cm^2, thus impeding hole injection toward GOR. These results were compared with the E_{cat}–J plot in DWE measurements, in which differential resistance dE_{cat}/dJ was found by fitting the slope in the region above the onset potential. At pH = 2, the Bi-rich layer reduced the differential resistance of $BiVO_4$ from 49 to 19 Ω cm^2 (Figure 3d), whereas it increased the differential resistance from 111 to 282 Ω cm^2 at pH = 9 (Figure 3e). While the dE_{cat}/dJ values were lower than the R_{ct} values from PEIS, they show consistent trends.

These data thus show DWE measurements provide a way to separate the steady-state catalytic activity from sem|cat interface charge-separation characteristics in this system. The results show that although both surfaces are formed from similar V dissolution by photocorrosion, the Bi-rich layer plays opposite roles in charge-transfer depending on the pH. When the catalytic rate is lower, durability is worse, which is consistent with the surface chemistry controlling the branching ratio between corrosion and productive GOR for photogenerated holes.

Acidic GOR performance of the Bi-rich/$BiVO_4$ photoanode was evaluated in a pH = 2 buffer solution with 0.10 M glycerol. The Bi-rich/$BiVO_4$ formed after the 1-h operation exhibited an increased photocurrent density of 4.7 mA cm^{-2} at 1.23 V_{RHE}, relative to the pristine $BiVO_4$ of 3.5 mA cm^{-2} (Figure 4a). Unlike conventional cocatalysts that are intentionally deposited on $BiVO_4$,

the Bi-rich layer generated via surface reconstruction could also be affected by trace elements naturally contained in the electrolyte.[54] In XPS analysis, nickel or iron, which expedites the reaction kinetics of typical oxidation reactions, was not detected on the surface of the Bi-rich layer. (Figure S25). Thus, considering the DWE analysis, the Bi-rich layer appears to perform efficient catalysis for acidic GOR by facilitating interfacial charge injection from $BiVO_4$.

Quantitative analysis using high-performance liquid chromatography (HPLC) was conducted to investigate the products of acidic GOR. Both $BiVO_4$ and Bi-rich/$BiVO_4$ generated multiple main products, including dihydroxyacetone (DHA), glyceraldehyde (GLAD), glyceric acid (GLA), glycolic acid (GCA), and formic acid (FA) (Figure S26), as reported in previous studies.[32,38] The glycolaldehyde peak was negligible and was excluded from the quantification of products.[44] The major product at pH = 2 was DHA, which is the highest value-added product in GOR (Figure S27).[55] The selectivity of DHA was increased from 48% of $BiVO_4$ to 53% of Bi-rich/$BiVO_4$. This increase appears to be related to the preferential exposure of Bi sites on the surface by the dissolution of V, since Bi-rich surfaces have been reported to promote the selective electrostatic adsorption of the secondary hydroxyl group in glycerol, thereby leading to favorable DHA formation.[36] The improved charge injection and consequent increase in photocurrent density through the Bi-rich layer enhanced the DHA production rate of $BiVO_4$ by about 1.5 times, from 178 to 270 mmol m^{-2} h^{-1}.

To evaluate the durability of $BiVO_4$, chronoamperometry was performed at 1.23 V_{RHE}, and product analysis for GOR was conducted in 1-h intervals for a 5-h span (Figure 4b). Based on the catalytic activity of the Bi-rich shell for acidic GOR, the Bi-rich/$BiVO_4$ photoanode operated stably for approximately 20 h. Initially, DHA formation is predominant, after which FA generation by C–C cleavage becomes more pronounced. In terms of the production of C_3 compounds (DHA

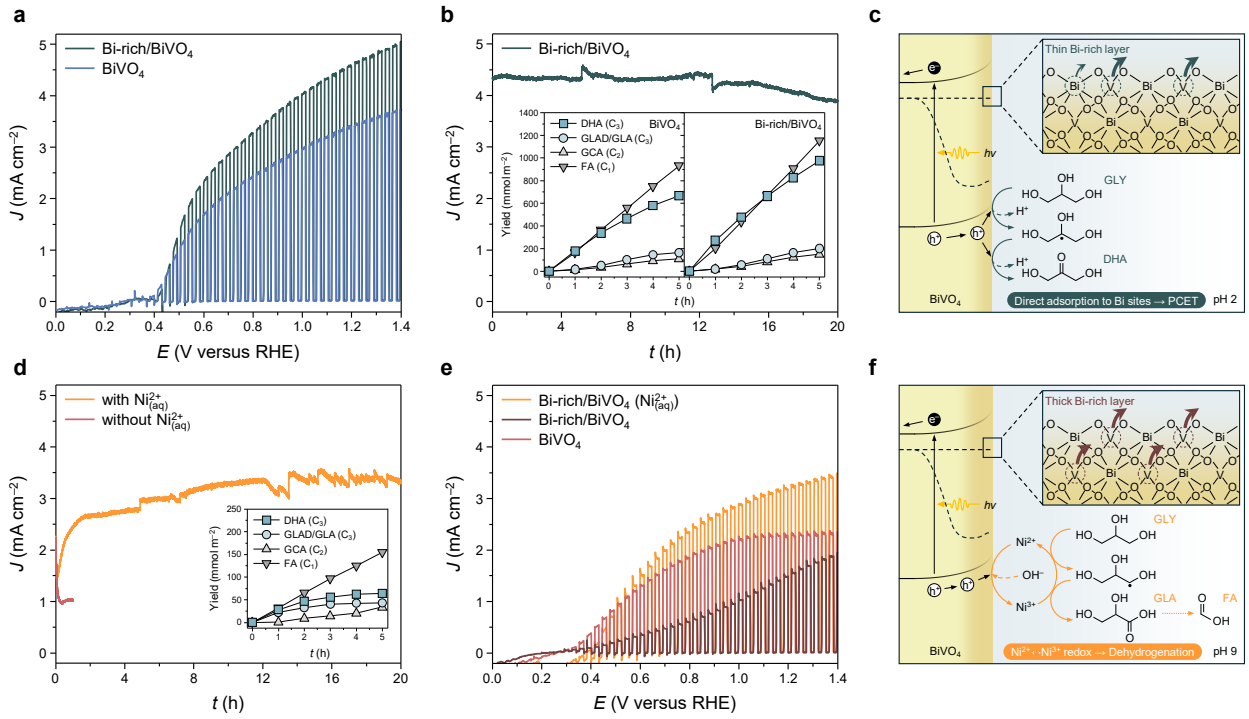

Figure 4. Acidic and alkaline glycerol oxidation of Bi-rich/$BiVO_4$ photoanodes. (a) *J–E* plots of $BiVO_4$ and Bi-rich/$BiVO_4$ photoanodes in a pH = 2 solution with 0.10 M glycerol. (b) *J–t* plot of Bi-rich/$BiVO_4$ photoanode and time-dependent yields of glycerol oxidation products for $BiVO_4$ and Bi-rich/$BiVO_4$ photoanodes at 1.23 V_{RHE} in a pH = 2 buffer solution with 0.10 M glycerol. (c) Schematic illustration of Bi-rich layer formation and reaction mechanism in acidic glycerol oxidation. (d) *J–t* plots and time-dependent yields of glycerol oxidation product for $BiVO_4$ photoanodes at 1.23 V_{RHE} in a pH = 9 (with 0.10 M glycerol) with and without 1.0 μM $Ni^{2+}_{(aq)}$. (e) *J–E* plots of $BiVO_4$ and Bi-rich/$BiVO_4$ photoanodes in a pH = 9 buffer solution (with 0.10 M glycerol) with and without 1.0 μM $Ni^{2+}_{(aq)}$. (f) Schematic illustration of Bi-rich layer formation and reaction mechanism in alkaline glycerol oxidation. All measurements were conducted under AM1.5G 1 sun illumination.

and GLAD/GLA), Bi-rich/$BiVO_4$ showed a higher C_3 yield of 1170 mmol m^{-2} than pristine $BiVO_4$ (830 mmol m^{-2}) after 5 h of operation.

Figure 4c summarizes the proposed mechanism by which the $BiVO_4$ photoanode operates stably in acidic GOR without a cocatalyst. At pH = 2, both Bi and V are expected to leach based on thermodynamics, but the faster dissolution rate of V over Bi results in the formation of a thin Bi-rich layer on $BiVO_4$. Bi sites are thought to be favorable for the glycerol adsorption as a Lewis-acidic center that interacts with hydroxyl groups.[28] While the VO_4 units in pristine $BiVO_4$ limit accessibility to surface Bi sites, preferential V dissolution exposes Bi sites, promoting activity

during GOR by proton-coupled electron transfer (PCET).[56] Increasing the density of accessible Bi sites appears to favor oxidation of the secondary hydroxyl group, contributing to kinetics through its fast two-electron pathway.[36,57] Consequently, it is likely that the operation-induced Bi-rich surface not only increases DHA selectivity but also lowers the surface hole-transfer resistance for the GOR, thereby contributing to the stability of acidic GOR.

Alkaline GOR performance of the Bi-rich/$BiVO_4$ photoanode was also evaluated in a pH = 9 buffer solution with 0.10 M glycerol. Since $BiVO_4$ exhibited poor stability in alkaline media (Figure 1b), achieving stable alkaline GOR required an alternative approach. We hypothesized that introducing Ni^{2+} ions into the aqueous electrolyte could stabilize $BiVO_4$ for GOR by providing surface-adsorbed $Ni^{2+/3+}$. During the first hour of chronoamperometry, the formation of the Bi-rich layer led to a pronounced degradation, but photocurrent density was recovered and stabilized upon adding 1.0 μM $Ni^{2+}_{(aq)}$ midway through the test (Figure S28). $Ni^{2+}_{(aq)}$ in solution with OH^- undergoes oxidation to Ni^{3+} by holes under anodic bias for the GOR, and these Ni species are likely adsorbed on the photoanode surface during the reaction.[58] When the Ni catalyst is reduced back to Ni^{2+} upon reaction with glycerol, it is likely dissolved into the electrolyte. This approach is similar to those used to create dynamically stable water-oxidation catalysts under near-neutral conditions.[59,60] The observed stable operation for 20 h upon $Ni^{2+}_{(aq)}$ addition, after formation of the Bi-rich layer for 1 h, suggests that the Bi-rich layer does not block hole transport between $BiVO_4$ and the Ni catalysts (Figure S29). This interpretation is consistent with nearly identical *J–V* curves of $BiVO_4$ and Bi-rich/$BiVO_4$ in a pH = 9 buffer containing a hole scavenger, showing that the Bi-rich layer does not limit the hole transport (Figure S30).

Chronoamperometry and GOR product analysis of $BiVO_4$ were conducted at 1.23 V_{RHE} with 1.0 μM $Ni^{2+}_{(aq)}$ in the electrolyte (Figure 4d). The rapidly decayed photocurrent density at initial

stages quickly recovered, and the photoanode operated stably for 20 h. This indicates that the formation of the Bi-rich layer by photocorrosion precedes the generation of the Ni catalysts through the redox process of Ni ions. Subsequently, Ni-containing species deposit or adsorb on the surface-reconstructed layer during the reaction, enhancing charge transfer of Bi-rich/$BiVO_4$.

In a similar experiment conducted in the absence of glycerol, although some photocurrent density was recovered at early stages with $Ni^{2+}_{(aq)}$, the overall current density still decayed, showing that the stability of the catalyst differed from that of GOR (Figure S31). XPS analysis after the 20-h stability test revealed a distribution of Ni (and Fe) on the surface of Bi-rich/$BiVO_4$, indicating the added Ni and trace Fe impurities present in the electrolyte were deposited on the surface under the oxidative bias (Figure S32).

The Ni-mediated alkaline GOR had a different product distribution from the nominally Bi-only acidic GOR. While the DHA selectivity decreased from 53% to 34%, the selectivity of GLAD/GLA increased from 3.7% to 26.5%, suggesting that adsorption of the primary hydroxyl group is enhanced in alkaline environments (Figure S33). At pH = 9, FA was the major product, exhibiting a steadily increasing yield over 5 h, whereas the yields of the C_3 products plateaued at steady values. This behavior indicates that C–C cleavage of the C_3 products becomes dominant in the static H-cell over time, leading to further oxidation into the C_1 product.[44] After 5 h, the total yield of the C_3 products (107 mmol m^{-2}) was lower than that of the C_1 product (154 mmol m^{-2}).

As a result, the Bi-rich/$BiVO_4$ measured for 20 h in a pH = 9 electrolyte with $Ni^{2+}_{(aq)}$ exhibited an increased photocurrent density of 3.2 mA cm^{-2}, compared to pristine $BiVO_4$ of 2.3 mA cm^{-2} (Figure 4e). This contrasts with the Bi-rich/$BiVO_4$ without $Ni^{2+}_{(aq)}$, which displayed a 30% decrease in photocurrent density (1.6 mA cm^{-2}) along with a reduced pFF.

Figure 4f illustrates a possible mechanism by which the Ni-assisted $BiVO_4$ photoanode stably operates during alkaline GOR. At pH = 9, the predominant dissolution of V leads to the formation of a thick Bi-rich layer on $BiVO_4$, which hinders hole transfer for GOR and consequently reduces stability. The addition of Ni^{2+} ions stabilizes the $BiVO_4$ surface for alkaline GOR through OH^--mediated redox cycling with Ni^{3+}. The Ni catalyst formed on the surface induces the adsorption of the primary hydroxyl group of glycerol, enhancing the production of not only GLAD/GLA by dehydrogenation but also FA through C–C cleavage. The increased surface-charge-transfer resistance and resulting instability caused by the Bi-rich layer are thus mitigated by even trace amounts of Ni^{2+} ions that determine GOR selectivity.

In summary, we uncover how operation-induced surface reconstruction governs the photoelectrochemical stability of $BiVO_4$ photoanodes during glycerol oxidation across acidic and alkaline media. PEC measurements and *ex situ* characterizations collectively reveal that preferential V species dissolution forms a Bi-rich shell on $BiVO_4$ under both pH conditions, but its catalytic role in durability is dictated by the electrolyte environment. We study the sem|cat interface using *in situ* measurements with the DWE platform that independently measures E_{sem} and E_{cat}, providing information on photovoltage and interfacial charge-transfer resistance changes during operation. Under acidic conditions, a thin Bi-rich layer on $BiVO_4$ lowers surface resistance and increases the photovoltage. The reconstructed surface acts as an active GOR catalyst, promoting hole injection and enabling stable operation without added cocatalysts. Under alkaline conditions, a thick Bi-rich shell leads to rapid photocurrent decay due to inhibited hole transfer for GOR. DWE analysis shows that the Bi-rich layer increases surface resistance and reduces photovoltage. Introducing trace Ni^{2+} into the electrolyte changes the behavior without pre-

deposition of cocatalysts. The Ni catalyst formed on the Bi-rich layer by Ni^{2+}/Ni^{3+} redox cycling during operation restores the charge-transfer capability and enables more-durable alkaline GOR.

These findings reveal that the surface reconstruction is neither universally beneficial nor detrimental, and the surface kinetics and resulting durability are governed by interaction with the electrolyte environment. Namely, even without cocatalyst deposition, intrinsic elemental leaching, often considered a degradation pathway, can be harnessed to create self-forming catalytic interfaces during operation. This study also establishes DWE analysis as a useful diagnostic platform for evaluating how surface reconstruction affects photoelectrode stability.

ASSOCIATED CONTENT

Supporting Information

Supporting Information is available free of charge.

Fabrication process, XRD patterns, and SEM images of $BiVO_4$, *J–E* plots, OCP, and PEIS of $BiVO_4$ photoanodes, sequential chronoamperometric response of $BiVO_4$ photoanode in glycerol oxidation, XRD patterns and STEM images of Bi-rich/$BiVO_4$, DWE measurement setup, CV and E_{cat}–*t* plots in DWE measurement, XPS of Bi-rich/$BiVO_4$, HPLC of Bi-rich/$BiVO_4$ with Ni^{2+}, and *J–t* plots of Bi-rich/$BiVO_4$ with Ni^{2+}.

AUTHOR INFORMATION

Corresponding Authors

Ho Won Jang – Department of Materials Science and Engineering, Research Institute of Advanced Materials, Seoul National University, Seoul 08826, Republic of Korea; Advanced

Institute of Convergence Technology, Seoul National University, Suwon 16229, Republic of Korea; orcid.org/0000-0002-6952-7359; Email: hwjang@snu.ac.kr

Shannon W. Boettcher – Department of Chemical & Biomolecular Engineering and Department of Chemistry, University of California, Berkeley, CA 94720, United States; Energy Technologies & Systems Division, Lawrence Berkeley National Laboratory, Berkeley, CA 94720, United States; Oregon Center for Electrochemistry, Department of Chemistry and Biochemistry, University of Oregon, Eugene, OR 97403, United States; orcid.org/0000-0001-8971-9123; Email: boettcher@berkeley.edu

Authors

Jin Wook Yang – Department of Chemical & Biomolecular Engineering and Department of Chemistry, University of California, Berkeley, CA 94720, United States; Energy Technologies & Systems Division, Lawrence Berkeley National Laboratory, Berkeley, CA 94720, United States; Department of Materials Science and Engineering, Research Institute of Advanced Materials, Seoul National University, Seoul 08826, Republic of Korea; https://orcid.org/0009-0003-8872-1987

Hee Ryeong Kwon – Department of Materials Science and Engineering, Research Institute of Advanced Materials, Seoul National University, Seoul 08826, Republic of Korea

Dong Su Kim – Department of Chemical & Biomolecular Engineering and Department of Chemistry, University of California, Berkeley, CA 94720, United States; Energy Technologies & Systems Division, Lawrence Berkeley National Laboratory, Berkeley, CA 94720, United States

Nicole A. Sagui – Oregon Center for Electrochemistry, Department of Chemistry and Biochemistry, University of Oregon, Eugene, OR 97403, United States, Departments of Chemical & Biomolecular Engineering and Chemistry, University of California, Berkeley, CA 94720,

United States, Energy Technologies & Systems Division, Lawrence Berkeley National Laboratory, Berkeley, CA 94720, United States

Yun Jeong Hwang – Department of Chemistry, Seoul National University, Seoul 08826, Republic of Korea

Author Contributions

‡J.W.Y. and H.R.K. contributed equally. J.W.Y. and S.W.B. designed the study. J.W.Y. prepared samples, collected the electrochemical data, and wrote the manuscript. H.R.K. performed the material characterizations. D.S.K. supported experiments. N.A.S. conducted ICP-MS measurements. Y.J.H. provided HPLC. H.W.J. and S.W.B. supervised the project. The manuscript was written through the contributions of all authors. All authors have given approval to the final version of the manuscript.

Notes

The authors declare no competing financial interests.

ACKNOWLEDGMENTS

This work was primarily supported by the U.S. Department of Energy, Office of Science, Office of Basic Energy Sciences, Solar Photochemistry Program, under Award No. DE-SC0000195, through Lawrence Berkeley National Laboratory FWP CH25SolarPhoto under Contract No. DE-AC02-05CH11231 with the U.S. Department of Energy. The stability test of photoanodes was also supported by the Liquid Sunlight Alliance, which is funded by the U.S. Department of Energy, Office of Science, Office of Basic Energy Sciences, Fuels from Sunlight Hub under Award Number DE-SC0021266, through Lawrence Berkeley National Laboratory FWP CH20LiSA under Contract No. DE-AC02-05CH11231 with the U.S. Department of Energy. J.W.Y.

acknowledges the Sejong Science Fellowship (RS-2023-00213786) and Basic Science Research Program (RS-2026-25539512) through the National Research Foundation of Korea (NRF), funded by the Ministry of Science and ICT and the Ministry of Education, Republic of Korea. H.R.K. acknowledges the Sejong Science Fellowship (RS-2026-25497307) through NRF funded by the Ministry of Science and ICT, Republic of Korea.

REFERENCES

(1) Lewis, N. S. Toward cost-effective solar energy use. *Science* **2007**, *315* (5813), 798–801. DOI: 10.1126/science.1137014.

(2) Yin, J.; Molini, A.; Porporato, A. Impacts of solar intermittency on future photovoltaic reliability. *Nat. Commun.* **2020**, *11*, 4781. DOI:10.1038/s41467-020-18602-6.

(3) Grätzel, M. Photoelectrochemical cells. *Nature* **2001**, *414*, 338–344. DOI: 10.1038/35104607.

(4) Schichtl, Z. G.; Carvalho, O. Q.; Tan, J.; Saund, S. S.; Ghoshal, D.; Wilder, L. M.; Gish, M. K.; Nielander, A. C.; Stevens, M. B.; Greenaway, A. L. Chemistry of materials underpinning photoelectrochemical solar fuel production. *Chem. Rev.* **2025**, *125* (10), 4786–4839. DOI: 10.1021/acs.chemrev.4c00258.

(5) Hwang, Y. J.; Boukai, A.; Yang, P. High density *n*-Si/*n*-TiO_2 core/shell nanowire arrays with enhanced photoactivity. *Nano Lett.* **2009**, *9* (1), 410–415. DOI: 10.1021/nl8032763.

(6) Chakthranont, P.; Hellstern, T. R.; McEnaney, J. M.; Jaramillo, T. F. Design and fabrication of a precious metal-free tandem core–shell p^+n Si/W-doped $BiVO_4$ photoanode for unassisted water splitting. *Adv. Energy Mater.* **2017**, *7* (22), 1701515. DOI: 10.1002/aenm.201701515.

(7) Jung, G.; Moon, C.; Martinho, F.; Jung, Y.; Chu, J.; Park, H.; Hajijafarassar, A.; Nielsen, R.; Schou, J.; Park, J.; Vesborg, P. C. K.; Hansen, O.; Lee, Y. S.; Canulescu, S.; Shin, B. Monolithically integrated $BiVO_4$/Si tandem devices enabling unbiased photoelectrochemical water splitting. *Adv. Energy Mater.* **2023**, *13* (35) 2301235. DOI: 10.1002/aenm.202301235.

(8) Man, I. C.; Su, H. Y.; Calle-Vallejo, F.; Hansen, H. A.; Martínez, J. I.; Inoglu, N. G.; Kitchin, J.; Jaramillo, T. F.; Nørskov, J. K.; Rossmeisl, J. Universality in oxygen evolution electrocatalysis on oxide surfaces. *ChemCatChem* **2011**, *3* (7), 1159–1165. DOI: 10.1002/cctc.201000397.

(9) Guo, L. J.; Luo, J. W.; He, T.; Wei, S. H.; Li, S. S. Photocorrosion-limited maximum efficiency of solar photoelectrochemical water splitting. *Phys. Rev. Appl.* **2018**, *10* (6), 064059. DOI: 10.1103/PhysRevApplied.10.064059.

(10) Xiao, Y.; Fu, J.; Pihosh, Y.; Karmakar, K.; Zhang, B.; Domen, K.; Li, Y. Interface engineering for photoelectrochemical oxygen evolution reaction. *Chem. Soc. Rev.* **2025**, *54* (3), 1268–1317. DOI: 10.1039/d4cs00309h.

(11) Kuang, Y.; Yamada, T.; Domen, K. Surface and interface engineering for photoelectrochemical water oxidation. *Joule* **2017**, *1* (2), 290–305. DOI: 10.1016/j.joule.2017.08.004.

(12) Pan, Y.; Zhang, H.; Zhang, B.; Gong, F.; Feng, J.; Li, Z.; Zou, Z.; Xiao, R.; Chu, S. Renewable formate from sunlight, biomass and carbon dioxide in a photoelectrochemical cell. *Nat. Commun.* **2023**, *14*, 1013. DOI: 10.1038/s41467-023-36726-3.

(13) Kang, F.; Wang, Q.; Du, D.; Wu, L.; Cheung, D. W. F.; Luo, J. Photoelectrochemical ethylene glycol oxidization coupled with hydrogen generation using metal oxide photoelectrodes. *Angew. Chem.* **2025**, *64* (5), 202417648. DOI: 10.1002/ange.202417648.

(14) Cha, H. G.; Choi, K. Combined biomass valorization and hydrogen production in a photoelectrochemical cell. *Nat. Chem.* **2015**, *7*, 328–333. DOI: 10.1038/nchem.2194.

(15) Yang, F.; Hanna, M. A.; Sun, R. Value-added uses for crude glycerol–a byproduct of biodiesel production. *Biotechnol. Biofuels* **2012**, *5*, 13. DOI: 10.1186/1754-6834-5-13.

(16) Kwon, H. R.; Yang, J. W.; Jang, H. W. Photoelectrocatalytic transformations of waste into value. *Artif. Photosynth.* **2025**, *1* (6), 267–292. DOI: 10.1021/aps.4c00028.

(17) Lin, J.; Roh, I.; Yang, P. Photochemical diodes for simultaneous bias-free glycerol valorization and hydrogen evolution. *J. Am. Chem. Soc.* **2023**, *145* (24) 12987–12991. DOI: 10.1021/jacs.3c01982.

(18) Kim, S.; Oh, D.; Jang, J. Unassisted photoelectrochemical H_2O_2 production with *in situ* glycerol valorization using α-Fe_2O_3. *Nano Lett.* **2024**, *24* (17), 5146–5153. DOI: 10.1021/acs.nanolett.3c05136.

(19) Andrei, V.; Roh, I.; Lin, J. A.; Lee, J.; Shan, Y.; Lin, C. K.; Shelton, S.; Reisner, E.; Yang, P. Perovskite-driven solar C_2 hydrocarbon synthesis from CO_2. *Nat. Catal.* **2025**, *8*, 137–146. DOI: 10.1038/s41929-025-01292-y.

(20) Han, C.; Li, C.; Yuwono, J. A.; Liu, Z.; Sun, K.; Wang, K.; He, G.; Huang, J.; Kumar, P. V; Vongsvivut, J.; Cong, J.; Mehrvarz, H.; Han, Z.; Lu, X.; Pan, J.; Hao, X.; Amal, R. Nanostructured hybrid catalysts empower the artificial leaf for solar-driven ammonia production from nitrate. *Energy Environ. Sci.* **2024**, *17* (15), 5653–5665. DOI: 10.1039/D3EE03836J.

(21) Guo, X.; Gao, R.; Ren, S.; Nguyen, N. T.; Chen, H.; Wu, L.; Wang, L. Direct ammonia and dihydroxyacetone production in an unbiased photoelectrochemical cell. *Nat. Commun.* **2025**, *16*, 6220. DOI: 10.1038/s41467-025-61080-x.

(22) Feng, X.; Sun, T.; Feng, X.; Yu, H.; Yang, Y.; Chen, L.; Zhang, F. Single-atomic-site platinum steers middle hydroxyl selective oxidation on amorphous/crystalline homojunction for photoelectrochemical glycerol oxidation coupled with hydrogen generation. *Adv. Funct. Mater.* **2024**, *34* (26), 2316238. DOI: 10.1002/adfm.202316238.

(23) Xie, Z.; Liu, X.; Jia, P.; Zou, Y.; Jiang, J. Facile construction of a $BiVO_4$/CoV-LDHs/Ag photoanode for enhanced photo-electrocatalytic glycerol oxidation and hydrogen evolution. *Energy Adv.* **2023**, *2* (9), 1366–1374. DOI: 10.1039/d3ya00215b.

(24) Wang, Q.; Ma, X.; Wu, P.; Li, B.; Zhang, L.; Shi, J. CoNiFe-LDHs decorated Ta_3N_5 nanotube array photoanode for remarkably enhanced photoelectrochemical glycerol conversion coupled with hydrogen generation. *Nano Energy* **2021**, *89* (A), 106326. DOI: 10.1016/j.nanoen.2021.106326.

(25) Balog, Á.; Kecsenovity, E.; Samu, G. F.; He, J.; Fekete, D.; Janáky, C. Paired photoelectrochemical conversion of CO_2/H_2O and glycerol at high rate. *Nat. Catal.* **2024**, *7*, 522–535. DOI: 10.1038/s41929-024-01134-3.

(26) Li, Y.; Kim, J.; Hong, W. T.; Kim, J. Y.; Lei, Q.; Han, H.; Baeck, U.; Kim, D. H.; Choi, C. H.; Kim, B.; Chung, C.; Kim, J. K. Highly selective photoelectrochemical glycerol valorization toward lactic acid with low-valence bimetallic overlayer on $CuWO_4$. *ACS Energy Lett.* **2025**, *10* (5), 2305–2314. DOI: 10.1021/acsenergylett.5c00551.

(27) Xiao, Y.; Wang, M.; Liu, D.; Gao, J.; Ding, J.; Wang, H.; Yang, H. Bin; Li, F.; Chen, M.; Xu, Y.; Xu, D.; Zhang, Y.; Fang, S.; Ao, X.; Wang, J.; Su, C.; Liu, B. Selective

photoelectrochemical oxidation of glycerol to glyceric acid on (002) facets exposed WO_3 nanosheets. *Angew. Chem.* **2024**, *136* (11), 202319685. DOI: 10.1002/ange.202319685.

(28) Liu, D.; Liu, J.; Cai, W.; Ma, J.; Yang, H. Bin; Xiao, H.; Huang, Y.; Liu, B. Selective photoelectrochemical oxidation of glycerol to high value-added dihydroxyacetone. *Nat. Commun.* **2019**, *10*, 1779. DOI: 10.1038/s41467-019-09788-5.

(29) Yang, J. W.; Ji, S. G.; Jeong, C.; Kim, J.; Kwon, H. R.; Lee, T. H.; Lee, S. A.; Cheon, W. S.; Lee, S.; Lee, H.; Kwon, M. S.; Moon, J.; Kim, J. Y.; Jang, H. W. High-efficiency unbiased water splitting with photoanodes harnessing polycarbazole hole transport layers. *Energy Environ. Sci.* **2024**, *17* (7), 2541–2553. DOI: 10.1039/d3ee03353h.

(30) Yang, J. W.; Park, I. J.; Lee, S. A.; Lee, M. G.; Lee, T. H.; Park, H.; Kim, C.; Park, J.; Moon, J.; Kim, J. Y.; Jang, H. W. Near-complete charge separation in tailored $BiVO_4$-based heterostructure photoanodes toward artificial leaf. *Appl. Catal. B* **2021**, *293*, 120217. DOI: 10.1016/j.apcatb.2021.120217.

(31) Lee, M. G.; Yang, J. W.; Park, I. J.; Lee, T. H.; Park, H.; Cheon, W. S.; Lee, S. A.; Lee, H.; Ji, S. G.; Suh, J. M.; Moon, J.; Kim, J. Y.; Jang, H. W. Tailored $BiVO_4/In_2O_3$ nanostructures with boosted charge separation ability toward unassisted water splitting. *Carbon Energy* **2023**, *5* (6), 321. DOI: 10.1002/cey2.321.

(32) Lin, C.; Dong, C.; Kim, S.; Lu, Y.; Wang, Y.; Yu, Z.; Gu, Y.; Gu, Z.; Lee, D. K.; Zhang, K.; Park, J. H. Photo-electrochemical glycerol conversion over a Mie scattering effect enhanced porous $BiVO_4$ photoanode. *Adv. Mater.* **2023**, *35* (15), 2209955. DOI: 10.1002/adma.202209955.

(33) Wu, Z.; Ren, K.; Zhou, J.; Zhang, Y.; Qi, L. Orientation engineering of nanoporous $BiVO_4$ photoanodes toward boosted glycerol valorization and hydrogen generation. *Adv. Funct. Mater.* **2025**, *35* (24), 2418294. DOI: 10.1002/adfm.202418294.

(34) Vo, T.; Kao, C.; Kuo, J.; Chiu, C.; Chiang, C. Unveiling the crystallographic facet dependence of the photoelectrochemical glycerol oxidation on bismuth vanadate. *Appl. Catal. B* **2020**, *278*, 119303. DOI: 10.1016/j.apcatb.2020.119303.

(35) Feng, X.; Feng, X.; Zhang, F. Enhanced photoelectrochemical oxidation of glycerol to dihydroxyacetone coupled with hydrogen generation via accelerative middle hydroxyl dehydrogenation over a Bi^0/Bi^{3+} interface of a cascade heterostructure. *J. Mater. Chem. A* **2023**, *11* (37), 20242–20253. DOI: 10.1039/d3ta04326f.

(36) Lu, Y.; Lee, B. G.; Lin, C.; Liu, T.; Wang, Z.; Miao, J.; Oh, S. H.; Kim, K. C.; Zhang, K.; Park, J. H. Solar-driven highly selective conversion of glycerol to dihydroxyacetone using surface atom engineered $BiVO_4$ photoanodes. *Nat. Commun.* **2024**, *15*, 5475. DOI: 10.1038/s41467-024-49662-7.

(37) Tateno, H.; Chen, S.; Miseki, Y.; Nakajima, T.; Mochizuki, T.; Sayama, K. Photoelectrochemical oxidation of glycerol to dihydroxyacetone over an acid-resistant Ta:$BiVO_4$ photoanode. *ACS Sustainable Chem. Eng.* **2022**, *10* (23) 7586–7594. DOI: 10.1021/acssuschemeng.2c01282.

(38) Liu, Y.; Shang, H.; Zhang, B.; Yan, D.; Xiang, X. Surface fluorination of $BiVO_4$ for the photoelectrochemical oxidation of glycerol to formic acid. *Nat. Commun.* **2024**, *15*, 8155. DOI: 10.1038/s41467-024-52161-4.

(39) Wu, Z.; Guo, H.; Ren, K.; Wang, Y.; Zhang, H.; Zhang, F.; Liu, L.; Li, G.; Qi, L. Photoelectrochemical glycerol valorization achieving an internal quantum efficiency over 180 % via current doubling. *Adv. Mater.* **2025**, 16504. DOI: 10.1002/adma.202516504.

(40) Sun, H.; Tang, R.; Wang, L.; Liang, Y.; Yang, W.; Lin, Z.; Zhang, X.; Chen, K.; Liang, W.; Zhao, S.; Zheng, R.; Huang, J. Vacancy-engineered bismuth vanadate for photoelectrocatalytic glycerol oxidation with simultaneous hydrogen production. *EES Catal.* **2025**, *3* (3), 337–346. DOI: 10.1039/d4ey00211c.

(41) Cui, J.; Li, T.; Yin, Z.; Chen, L.; Wang, J. Remarkably enhanced acidic photoelectrochemical glycerol oxidation achieving the theoretical maximum photocurrent of $BiVO_4$ through anion modulation. *Chem. Eng. J.* **2024**, *493*, 152461. DOI: 10.1016/j.cej.2024.152461.

(42) Kong, H.; Gupta, S.; Pérez-Torres, A. F.; Höhn, C.; Bogdanoff, P.; Mayer, M. T.; Krol, R.; Favaro, M.; Abdi, F. F. Electrolyte selection toward efficient photoelectrochemical glycerol oxidation on $BiVO_4$. *Chem. Sci.* **2024**, 15, 10425–10435. DOI: doi.org/10.1039/d4sc01651c.

(43) Zeng, G.; Pham, T. A.; Vanka, S.; Liu, G.; Song, C.; Cooper, J. K.; Mi, Z.; Ogitsu, T.; Toma, F. M. Development of a photoelectrochemically self-improving Si/GaN photocathode for efficient and durable H_2 production. *Nat. Mater.* **2021**, *20* (8), 1130–1135. DOI: 10.1038/s41563-021-00965-w.

(44) Hilbrands, A. M.; Goetz, M. K.; Choi, K. C−C bond formation coupled with C−C bond cleavage during oxidative upgrading of glycerol on a nanoporous $BiVO_4$ photoanode. *J. Am. Chem. Soc.* **2023**, *145* (46), 25383–25391. DOI: 10.1021/jacs.3c09631.

(45) Lee, D. K.; Choi, K. Enhancing long-term photostability of $BiVO_4$ photoanodes for solar water splitting by tuning electrolyte composition. *Nat. Energy*, **2018**, *3*, 53–60. DOI: 10.1038/s41560-017-0057-0.

(46) Pei, H.; Peng, L.; Jiang, Z.; Zhang, Y.; Li, R.; Peng, T. Gradient-tuned VO_4 vacancies in $BiVO_4$ photoanode for boosting bulk hole transport and oxygen evolution reaction performance. *Adv. Funct. Mater.* **2024**, *34* (30), 2401122. DOI: 10.1002/adfm.202401122.

(47) Wang, S.; Li, C.; Qi, Y.; Zhang, J.; Wang, N.; Liu, M.; Zhang, B.; Cai, X.; Zhang, H.; Wei, S.; Ma, G.; Yang, J.; Chen, S.; Zhang, F. Etched $BiVO_4$ photocatalyst with charge separation efficiency exceeding 90%. *Nat. Commun.* **2025**, *16*, 3776. DOI: 10.1038/s41467-025-59076-8.

(48) Tang, T.; Li, Z.; Zhou, L.; Zhang, P.; Cheng, Y. F.; Liang, Y.; Zhuang, J. H.; Hu, X. Y.; Ma, Q. J.; Zhang, B. Y.; Jannat, A.; Ou, J. Z. Tunable synthesis of 2D bismuth oxyhydroxide and oxysulfide from solid–liquid interfacial reaction for high performance optoelectronic gas sensing. *Small* **2025**, *21* (17), 2411522. DOI: 10.1002/smll.202411522.

(49) Toma, F. M.; Cooper, J. K.; Kunzelmann, V.; Mcdowell, M. T.; Yu, J.; Larson, D. M.; Borys, N. J.; Abelyan, C.; Beeman, J. W.; Yu, K. M.; Yang, J.; Chen, L.; Shaner, M. R.; Spurgeon, J.; Houle, F. A.; Persson, K. A.; Sharp, I. D. Mechanistic insights into chemical and photochemical transformations of bismuth vanadate photoanodes. *Nat. Commun.* **2016**, *7*, 12012. DOI: 10.1038/ncomms12012.

(50) Yao, X.; Zhao, X.; Chen, Z.; Yao, X.; Zhao, X.; Hu, J.; Xie, H.; Wang, D.; Cao, X.; Zhang, Z.; Huang, Y.; Chen, Z.; Sritharan, T. The self-passivation mechanism in degradation of $BiVO_4$ photoanode. *iScience* **2019**, *19*, 976–985. DOI: 10.1016/j.isci.2019.08.037.

(51) Qiu, J.; Hajibabaei, H.; Nellist, M. R.; Laskowski, F. A. L.; Hamann, T. W.; Boettcher, S. W. Direct *in situ* measurement of charge transfer processes during photoelectrochemical water oxidation on catalyzed hematite. *ACS Cent. Sci.* **2017**, *3* (9), 1015–1025. DOI: 10.1021/acscentsci.7b00310.

(52) Lin, F.; Boettcher, S. W. Adaptive semiconductor/electrocatalyst junctions in water-splitting photoanodes. *Nat. Mater.* **2014**, *13*, 81–86. DOI: 10.1038/nmat3811.

(53) Lee, D.; Wang, W.; Zhou, C.; Tong, X.; Liu, M.; Galli, G.; Choi, K. S. The impact of surface composition on the interfacial energetics and photoelectrochemical properties of $BiVO_4$. *Nat. Energy* **2021**, *6,* 287–294. DOI: 10.1038/s41560-021-00777-x.

(54) Trotochaud, L.; Young, S. L.; Ranney, J. K.; Boettcher, S. W. Nickel−iron oxyhydroxide oxygen-evolution electrocatalysts: The role of intentional and incidental iron incorporation. *J. Am. Chem. Soc.* **2014**, *136* (18), 6744–6753. DOI: 10.1021/ja502379c.

(55) Pagliaro, M.; Ciriminna, R.; Kimura, H.; Rossi, M.; Pina, C. D. From glycerol to value-added products. *Angew. Chem.* **2007**, *46* (24), 4434–4440. DOI: 10.1002/anie.200604694.

(56) Kusama, H.; Sayama, K. Mechanism of glycerol oxidation on bismuth vanadate photoanodes: Influence of tantalum doping. *J. Photochem. Photobiol. A* **2025**, *460*, 116143. DOI: 10.1016/j.jphotochem.2024.116143.

(57) Kwon, Y.; Birdja, Y.; Spanos, I.; Rodriguez, P.; Koper, M. T. M. Highly selective electro-oxidation of glycerol to dihydroxyacetone on platinum in the presence of bismuth. *ACS Catal.* **2012**, *2* (5), 759–764. DOI: 10.1021/cs200599g.

(58) Thorarinsdottir, A. E.; Veroneau, S. S.; Nocera, D. G. Self-healing oxygen evolution catalysts. *Nat. Commun.* **2022**, *13*, 1243. DOI: 10.1038/s41467-022-28723-9.

(59) Kanan, M. W.; Nocera, D. G. In situ formation of an oxygen-evolving catalyst in neutral water containing phosphate and Co^{2+}. *Science* **2008**, *321*, 1072–1075. DOI: 10.1126/science.1162018.

(60) Chung, D. Y.; Lopes, P. P.; Farinazzo Bergamo Dias Martins, P.; He, H.; Kawaguchi, T.; Zapol, P.; You, H.; Tripkovic, D.; Strmcnik, D.; Zhu, Y.; Seifert, S.; Lee, S.; Stamenkovic, V. R.; Markovic, N. M. Dynamic stability of active sites in hydr(oxy)oxides for the oxygen evolution reaction. *Nat. Energy* **2020**, *5* (3), 222–230. DOI: 10.1038/s41560-020-0576-y.

TOC

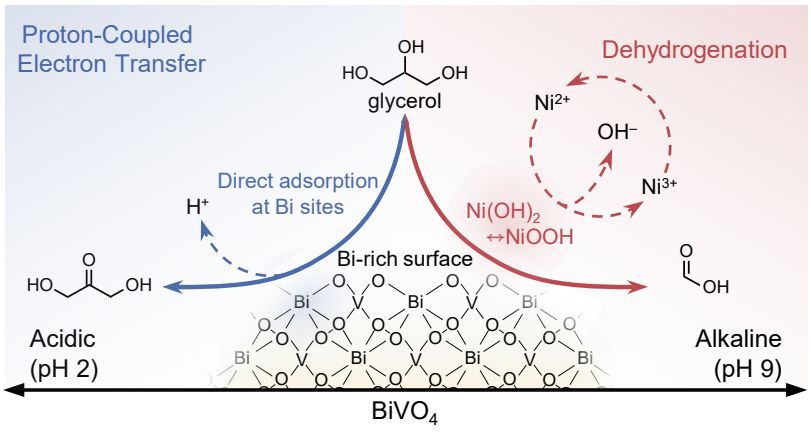
Proton-Coupled
Electron Transfer
Dehydrogenation
glycerol
Ni2+
OH−
Ni3+
Direct adsorption
at Bi sites
H+
Ni(OH)2
↔NiOOH
Bi-rich surface
Acidic
(pH 2)
Alkaline
(pH 9)
BiVO4